Corrosion Science 225 (2023) 111618

Contents lists available at ScienceDirect

Corrosion Science

journal homepage: www.elsevier.com/locate/corsci

Dense Cr/GLC multilayer coating by HiPIMS technique in high hydrostatic pressure: Microstrusctural evolution and galvanic corrosion failure

Shuyu Li [a,b], Hao Li [a], Guanshui Ma [a,*], Jing Wei [a], Guangxue Zhou [a], Yan Zhang [a], Peng Guo [a,*], Peiling Ke [a,b], Aiying Wang [a,b,**]

[a] Key Laboratory of Marine Materials and Related Technologies, Zhejiang Key Laboratory of Marine Materials and Protective Technologies, Ningbo Institute of Materials Technology and Engineering, Chinese Academy of Sciences, Ningbo 315201, PR China
[b] Center of Materials Science and Optoelectronics Engineering, University of Chinese Academy of Sciences, Beijing 100049, PR China

ARTICLE INFO

Keywords:
Cr/GLC multilayer coatings
HiPIMS
Electrochemical behavior
Interface galvanic corrosion

ABSTRACT

The dense Cr/GLC multilayer coatings were fabricated by high power impulse magnetron sputtering (HiPIMS) with various duty cycles. HiPIMS-deposited GLC coatings with high density displayed the lower corrosion current density by five times than DC- deposited GLC, due to the higher C^+ ionization rate and larger incident ions energy. Noted that, after 425 h immersion with 15 MPa, though a laminar-like spallation occurred in the Cr/GLC interfaces instead of the coating/substrate interfaces, the lower galvanic corrosion current density was particularly achieved at 2.04×10^{-9} A·cm^{-2} for the HiPIMS-coatings with reduced porosity, emulating an excellent tolerance of long-term corrosion resistance for deep-sea.

1. Introduction

With the marine exploration becoming increasingly intensive, more and more key mechanical components used in deep-sea instruments and station platforms are apt to be worn due to the heavy hydraulic friction with severe seawater corrosion [1,2]. Particularly, when the structured materials made of steels or other metallic alloys are exposed to the aggressive chloride constituents, the corrosion will be accelerated rapidly, which is very fatal to the durability and safety of marine systems [3]. One of the popular solutions is to promote the formation of passive films generated over metallic surface and tailor their properties by additive chemical compositions, such as doping Cr, Ni and C to steels, etc. [4–6]. Taking concerns for the required superior tribo-corrosion performance with long-lasting lifetime, furthermore, surface coating technology is alternatively considered as the most promising strategy to inhibit the corrosive deterioration and premature failure of metallic components in natural seawater [7,8]. Specifically, amorphous carbon (a-C) coatings, a class of metastable carbon materials composed of hybrid C-sp^3 and C-sp^2 atomic bonds, have drawn much attention as the intelligent and protective candidates due to their combinational properties of high hardness, low friction coefficient and wear rate, as well as good chemical inertness [9,10]. Moreover, the wide variety of a-C coatings favors the facile synthesis to meet the different demands, where the empirical synonyms of a-C coatings are classified with the terms of hydrogenated amorphous carbon (a-C:H), graphite-like carbon (GLC), tetrahedral amorphous carbon (ta-C) and diamond-like carbon (DLC) base on the ratio of sp^2/sp^3 content and hydrogen additives in a-C matrix [9].

Among the family of a-C coatings, many studies have reported that GLC presents the most interesting characteristics to suppress both tribological damage and severe corrosion induced by Cl^- solutions [11]. For example, an observation was that the coefficient of friction (COF) for GLC coatings was less than 0.1 whatever the changes in friction pairs, in which the best capability for tribo-corrosion resistance was gained in sliding against Si_3N_4 and SiC [12]. The reason could be that the densely amorphous GLC coating significantly inhibited the penetration of corrosive medium to substrate. However, GLC coatings prepared by various physical vapor deposition (PVD) techniques [13] generally possess the various intrinsic defects in structure, such as pinholes, nodular particles, and penetrating cracks. These defects in turn easily stimulate the tribological and corrosive failure under highly hydrostatic pressure. By introducing the multilayered Cr/GLC structure, Li et al. [14] found the

* Corresponding authors.
** Corresponding author at: Key Laboratory of Marine Materials and Related Technologies, Zhejiang Key Laboratory of Marine Materials and Protective Technologies, Ningbo Institute of Materials Technology and Engineering, Chinese Academy of Sciences, Ningbo 315201, PR China.
E-mail addresses: maguanshui@nimte.ac.cn (G. Ma), guopeng@nimte.ac.cn (P. Guo), aywang@nimte.ac.cn (A. Wang).

https://doi.org/10.1016/j.corsci.2023.111618
Received 4 September 2023; Received in revised form 6 October 2023; Accepted 24 October 2023
Available online 26 October 2023

open pinholes for media penetration were dramatically reduced, and the COF during corrosive-friction test reached a very low value of 0.046, replying the excellent tribo-corrosion resistance of Cr/GLC coating. In addition, to restrain the crater-like failure originated from the macro-particle defects during coating growth, Liu et al. [15] conducted the extra cleaning process to improve the density of GLC, in which the coating porosity was significantly decreased from 5.2% to 2.54% and the corrosion resistance was improved as expectation.

Different with the traditional magnetron sputtering and cathodic arc evaporation for GLC synthesis, high power impulse magnetron sputtering (HiPIMS) has drawn much attention as a new sputtering PVD technique very recently. Especially, HiPIMS performs the combined both advantages of magnetron sputtering and arc evaporation, but without their respective disadvantages [16,17]. Thereafter, HiPIMS can ideally emulate the high ionization rate of targets and high incident ion energy as those of cathodic arc deposition, and simultaneously offers the smooth surface and dense deposition as those of sputtering. Qureshi et al. [18] prepared Cr_2AlC coating by DC magnetron sputtering (DCMS) and HiPIMS for comparison. They found that the DCMS-deposited coating displayed an obviously coarse columnar structure with size of 250–500 nm, while a dense and columnar-free smooth coating with enhanced mechanical properties was observed in HiPIMS deposition process. The even more observation was that, due to the highly ionized plasma with high kinetic energy bombardment, HiPIMS promoted the formation of nanocrystalline $TiAl_x$ compounds, which further led to the dense and smooth Ti_3AlC_2 coating at 700 °C, while Ti_2AlC coating was only obtained by DCMS technique [19]. Similarly, the improvement of structural density and mechanical properties was also observed in WC-DLC films. As state above, it is very likely that introducing HiPIMS deposition can facilitate the growth of GLC coatings with highly dense and smooth defect-free structure, which is of great importance for the long-lasting tribo-corrosion durability under deep sea conditions [20,21].

In this work, we specially fabricated a series of dense Cr/GLC multilayer coatings by a home-made hybrid HiPIMS technique composed of multi-target sputtering sources. The dependence of coating growth was investigated by the in-situ plasma characteristics during HiPIMS process with various duty cycles. The electrochemical behavior and structural evolution of deposited Cr/GLC coatings were studied from atmosphere to high hydrostatic pressure condition under different immersion times, emulating the harsh deep-sea environments. The corrosion failure was discussed in terms of the densification and interfacial galvanic corrosion in the multilayer Cr/GLC coatings. In order to address the effect of coating porosity on corrosion resistance, the DCMS procedure was also conducted for the GLC deposition with the same sputtering power and coating thickness for comparison.

2. Experimental section

2.1. Coating deposition

The Cr/GLC multilayered coatings were prepared by a home-made hybrid magnetron sputtering system, which composed of the rectangular DCMS source, HiPIMS source and linear ion source (Fig. 1(a)). The dimension for both chromium target (purity: 99.999%) and graphite target (purity: 99.99%) was about 380 mm × 100 mm × 7 mm. The mirror polished 17–4 PH stainless steel (Φ17 mm × 3 mm) couples and P-type (100) Si wafers were used as substrates. Before deposition, the substrates were ultrasonic cleaned in acetone for 20 min and then in anhydrous ethanol for 15 min. When the chamber was evacuated to below 4×10^{-5} Torr, all the loaded substrates were etched by Ar^+ ions discharged by a linear ion beam source for 40 min under a DC pulsed bias of − 200 V, in order to remove the contaminants or impurities adsorbed on the substrate surface [22]. After etching, a gradient Cr and Cr_xN layer with total thickness of 180 ± 20 nm was specifically deposited by HiPIMS source with a duty cycle of 10% and a pulse width of 200 μs [23]. During this process, the sputtering power was controlled at 1.7 kW and a negative bias of − 100 V was applied to substrate. Subsequently, the GLC layers with a thickness of 100 ± 20 nm were synthesized using HiPIMS and DCMS modes with the same power of 2 kW for comparison. The pulse widths for carbon discharge was changed at 150 μs, 200 μs, and 250 μs, corresponding to the duty cycles of 7.5%, 10%, and 12.5%, respectively. For easy description, the Cr/GLC multilayer coating was following named by HiPIMS deposited S7.5, S10, S12.5 and the comparative DC coated samples. During all the processes of coating deposition, the Ar gas with flow rate of 55 sccm was introduced to chamber and the working pressure was maintained at 2.0×10^{-3} Torr. The outmost thickness of Cr/GLC layer was optimized at 220 nm ± 20 nm to achieve more stronger durability of tribocorrosion resistance[14,22,24].

Furthermore, in order to clarify the difference of plasma discharge between DCMS and HiPIMS process for carbon ionization, the ion energy distribution functions (IEDFs) were particularly in-situ measured by a quadrupole mass spectrometer with an energy filter (HIDEN EQP 300). In the experimental process, the first stage of IEDFs was used to measure the chamber with base pressure of 4×10^{-5} Torr, which aimed to remove the effect of the background vacuum (RGA mode). During target discharges, the EQP probe started working, where the second step was operated with setting parameters (SIMS mode), e.g. magnification, energy etc. Based on this procedure, the distributed ionization, relevant to ion energy, could be elucidated during plasma discharges (SIMS: Mass and energy of ions generated in the plasmas; RGA: Mass and energy analysis of neutrals and radicals). Tests of the IEDFs for C^+ ion were used in the energy steps of 0.05 eV in time averaged mode. The dwell time was set as 1000 ms. The ion flux was calculated by integrating over the measured IEDFs. Fig. 1(b) shows the representative discharge curves of

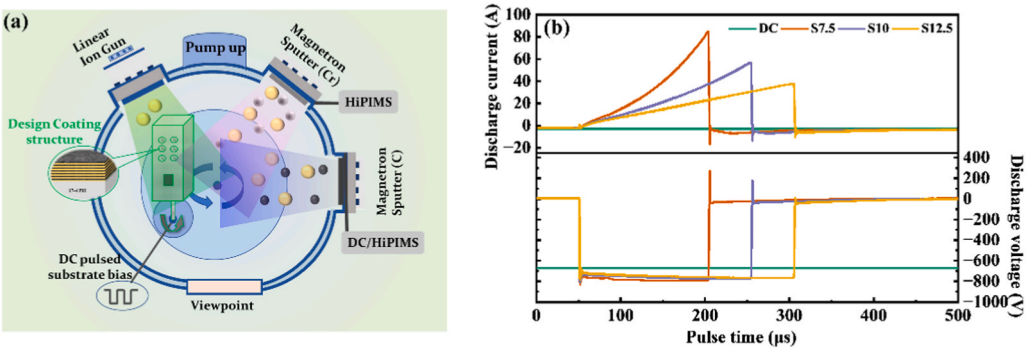

Fig. 1. (a) Schematic diagram of the hybrid deposition system for coatings. (b) Representative in-situ discharge curves of target voltage and discharge current during various magnetron sputtering processes.

sputtered-C for DC mode and HiPIMS mode, where the distinct square pulsed peaks occurred in all the HiPIMS curves with various duty cycles. Noted that increasing the duty cycle from 7.5% to 12.5% led to the decrease of discharge current from 84 A to 37.6 A during the HiPIMS processes, and the discharge voltage of 780 V∼748 V in HiPIMS mode was much higher than that of DC mode at 655 V. This observation could be assigned to the typical pulsed highest discharge voltage together with highest discharge current during HiPIMS technique, which was quite different with the high discharge voltage with lower current during DC sputtering.

2.2. Electrochemical and in-situ immersion tests

All electrochemical measurements were carried out in the simulated 3.5 wt.% NaCl solution. An electrochemical Reference 600 + workstation (Gamry, USA) using a three-electrode system (vs Ag/AgCl) was employed to characterize the open circuit potential (OCP), electrochemical impedance spectra (EIS), polarization curves, and galvanic corrosion current density. Particularly, the EIS measurements were conducted at potentiostatic mode with a perturbation voltage of 10 mV. The frequency was tailored from 100 kHz to 0.01 Hz. The fitting and analysis of simulated circuits in EIS using Zview software. Potentiodynamic polarization was tested with a speed of 1 $mV{\cdot}s^{-1}$, where the data analysis was performed using the software in workstation. To address the electrochemical behavior of coating under high hydraulic condition, the autoclave corrosion test system (CORTEST Inc. USA) was used for in-situ high pressure coupled with immersion test. Namely, the coatings were immersed in 3.5 wt.% NaCl solution and pressurized under 15 MPa to simulate the deep seawater of 1500 m, in which the other parameters of high hydrostatic pressure test were the same to those of the atmospheric test.

2.3. Characterization of coatings

The surface and cross-section morphology of deposited coatings were observed by scanning electron microscopy (SEM, FEI, Quanta 250 FEG, USA) at voltage of 10 kV. The Raman (Renishaw inVia-reflex, UK) with laser wavelength of 532 nm was conducted to elucidate the atomic carbon bond in the Cr/GLC coatings. The evolution of chemical compositions for various elements were analyzed by X-ray photoelectron spectroscopy (XPS, Thermo Scientific ESCALAB 250) with a monochromatic Al X-ray source. Before XPS test, the Ar^+ ions with energy of 2 keV were introduced to etch the surface for 30 s to eliminate the possible pollution and adsorbed oxygen. The hardness and elastic modulus were analyzed by nano-indentation with a continuous stiffness measurement mode (MTS-G 200). The indentation depth was 200 nm, and the average value of mechanical properties was selected in the stabilized loading region of 150–170 nm to avoid the contribution from substrate.

The density of the coatings was measured by X-ray reflection (XRR) using a Cu target Kα (λ = 1. 5418 nm) radiation source with a measurement angle range of 0–1.3°. The simulation was performed by a three-layer structure model of Si/SiC/GLC. Noted that a silicon carbide interface layer was added between the substrate and GLC, considering the heavy bombardment of HiPIMS-discharged C^+ ions favored the generation of SiC transitional layer on the Si substrate. By fitting the critical angle (θ_c) in the curve, the average density (ρ) could then be calculated according to the following formula [25–27].

$$\rho = \left[\frac{\pi\theta c^2}{N_A r_e \lambda^2}\right]\left[\frac{M_C}{Z_C}\right] \quad (1)$$

Where ρ was the density of coating, θ_c was the critical angle, N_A was the Avogadro constant (6.022×10^{23}), r_e was the electron-classical-radius with 2.818×10^{-15} m, λ was corresponded to the wavelength of X-ray at 1.5418 nm, M_c was the molar mass of the carbon atom, while Z_c was the atomic number of the carbon atoms.

3. Result and discussion

3.1. Microstructural characteristics of Cr/GLC coatings

Fig. 2 shows the surface topographies and cross-sectional morphologies of deposited Cr/GLC coatings with different duty cycles. Although there were tiny nodular defects in the coating surfaces, the coatings were distinctly smooth and dense regardless of the changes in duty cycles. The R_a of the DC, S7.5, S10, S12.5 were 19.2 nm, 11.4 nm, 14.5 nm, and 12.7 nm, respectively. Meantime, no crack or spallation emerged at the coating surfaces and interfaces, implying the strong interfacial bonding within coatings and substrate. Based on the evolutions of cross-sectional morphology, the typical periodic structure with alternated C layer and Cr layer was successfully fabricated in both DC and HiPIMS technique. However, it was worthy to note that DC-sputtered Cr/GLC multilayer coatings was about 200 nm thicker than those of HiPIMS-deposited coating samples, probably due to the re-sputtering arisen from the highly ionized ions with high kinetic energy in case of HiPIMS [16].

Raman spectroscopy is well known as an important non-destructive method to characterize the chemical bond state of amorphous carbon coatings [28]. Fig. 3(a) shows the Raman spectra of the Cr/GLC multilayered coatings with a wavelength range of 800–2000 cm^{-1} under different duty cycles. A distinct broad peak was visible as a sign of typical amorphous carbon regardless of increasing duty cycles. Since the carbon Raman spectroscopy could be deconvoluted into D-band peak at 1359 cm^{-1} and G-band peak at 1591 cm^{-1}, the intensity ratio of D peak to G peak (I_D/I_G) was closely related to the cluster size of sp^2 bonds. In addition, the position of G peak and the full width at half maximum of G peak (G-FWHM) could be used to observe the structural variations in a-C films. In current works, increasing the duty cycle from DC to the HiIPIMS-12.5% caused the slight changes in I_D/I_G with range of 3.6–3.75, together with a very small variation for both G-peak position. The G-FWHM raised slightly indicated the occurrence of structural disorder in the DLC, as well as the increase of internal stress (Fig. 3(b)) [29,30]. Therefore, the Raman analysis proposed that the atomic bond structure of carbon network in Cr/GLC coatings was not changed by the applied duty cycles during both DC and HiPIMS sputtering processes. Further evolution of chemical composition of GLC layer was conducted by XPS test as a function of the used duty cycles. As shown in Fig. 3(c), all the core XPS spectra of C 1 S were subsequently deconvoluted to three peaks, namely the sp^2 carbon(C═C) at 284.3 ± 0.2 eV, sp^3 carbon(C-C) at 285.2 ± 0.2 eV, and C-O/C═O at 286.5 ± 0.3 eV, respectively. When the duty cycle was increased from DC to HiPIMS pulsed 12.5%, both the C-sp^2 bonds and the C-sp^3 displayed a very small composition changes with a range of 7.4%–75.4% and 32.6–24.6%, respectively (Fig. 3d). This phenomenon implied that the weak dependence of carbon $sp^3$and sp^2 atomic bonds upon the introduced duty cycles during various sputtering depositions.

Considering the key effect of incident ions with kinetic energy during sputtering, XRR test was further undertaken to address the structure density beyond of the above-mentioned variation of carbon atomic bonds [31–33]. Fig. 4(a) shows the XRR curves for the GLC layers deposited under various duty cycles, where the oscillation patterns of experimental results were distinct. After fitting the patterns, all the HiPIMS deposited GLC coating rendered the higher density in a range of 2.62–2.49 g/cm^3 than that of DC coating at 2.46 g/cm^3. Most importantly, increasing the duty cycle from 7.5% to 12.5% led to a small decrease in coating density under the HiPIMS mode. The detailed implication of the used key parameters to conduct the data fitting was given in Table S1. Noted that the smaller χ^2 in the Table S1 generally reflected the better accuracy during result fitting.

Since it was known that the plasma discharge involving the ionization rate and kinetic energy could play key role in the coating deposition and thereafter the growth defects as well as the structural density, the

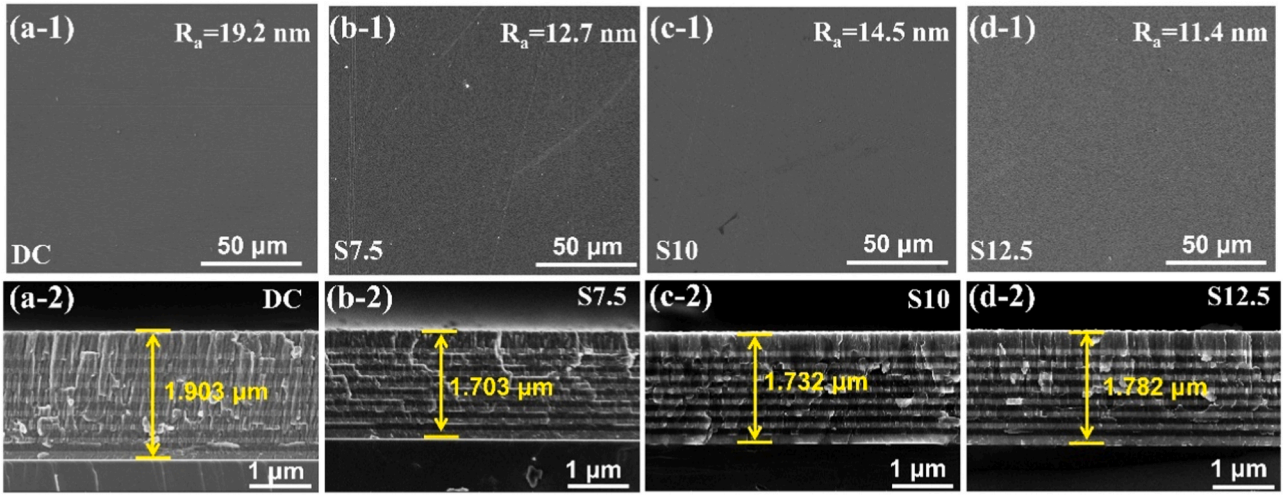

Fig. 2. Surface topographies and cross-sectional morphologies of the Cr/GLC coatings with different duty cycles.

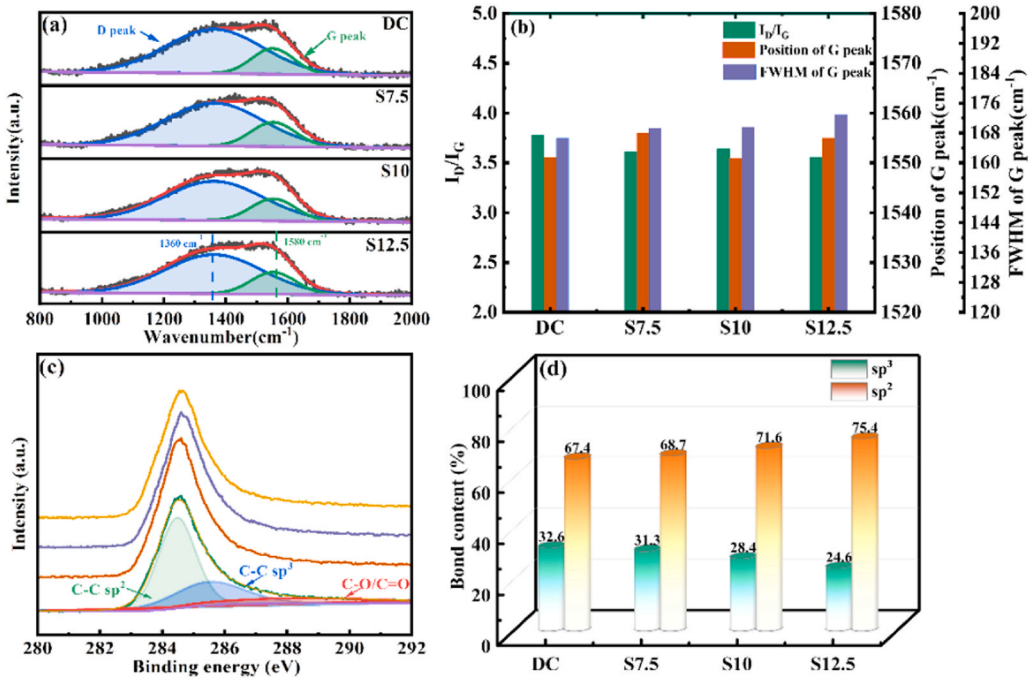

Fig. 3. (a) The Raman spectra, (b) the fitted I_D/I_G ratio, G peak position and FWHM of G-peak, (c) the C 1 s core level XPS spectra, and (d) the deconvoluted composition of carbon bonds in Cr/GLC coatings with different duty cycles.

mass spectrometer with an energy filter was specially conducted to elucidate the plasma characteristics and the IEDFs for the representative carbon ion species. As shown in Fig. 4(b), the distinct charged peaks with Ar^+ ions at molar mass of 40 g/mol and C^+ ions at 12 g/mol were identified as the dominant ions for both DC and HiPIMS modes. Meanwhile, even the intensity of Ar^+ ions were similar for both DC and HiPIMS cases, the intensity of C^+ ions in HiPIMS process was more distinct larger than that of DC state, demonstrating a higher ionization rate of carbon favored by HiPIMS technique. Fig. 4(c) shows the time averaged IEDFs of representative carbon ions with the various duty cycles for comparison. The IEDFs consisted of a lower peak at about 3 eV and a high energy tail traced up to 100 eV. By comparing the IEDFs curves, it was indeed that there was a distinct observation around the peak position at 3 eV. In general, direct electron impact ionization was the main mechanism for the generation of ions in plasmas. Taking the concept of plasma diagnostics in magnetron sputtering, the distinct peak around 3 eV could be originated from the suddenly temporary increase in ion energy when the thermalized ions were accelerated and transferred from the plasma sheath region to the substrate nearby for coating deposition. The energy distribution of ions generated by direct electron impact ionization was coincident to a Maxwell distribution under the thermal equilibrium or local thermal equilibrium conditions. This observation was quite common for the plasma discharges in most magnetron sputtering techniques [34]. Compared with the intensity variations, one observation was that all the absolute intensities of IEDFs in HiPIMS were much larger than that of DCMS, implying the higher ionization rate together with higher kinetic energy. Another attention was that the there was a slight variation in IEDFs intensity with changing duty cycles, where increasing duty cycle in range of 7.5%–12.5% led to a tiny decrease in the IEDFs intensity. Combined with the characteristics of plasma discharge, it could be concluded that HiPIMS technique benefited a higher ionization rate of carbon target and a larger kinetic

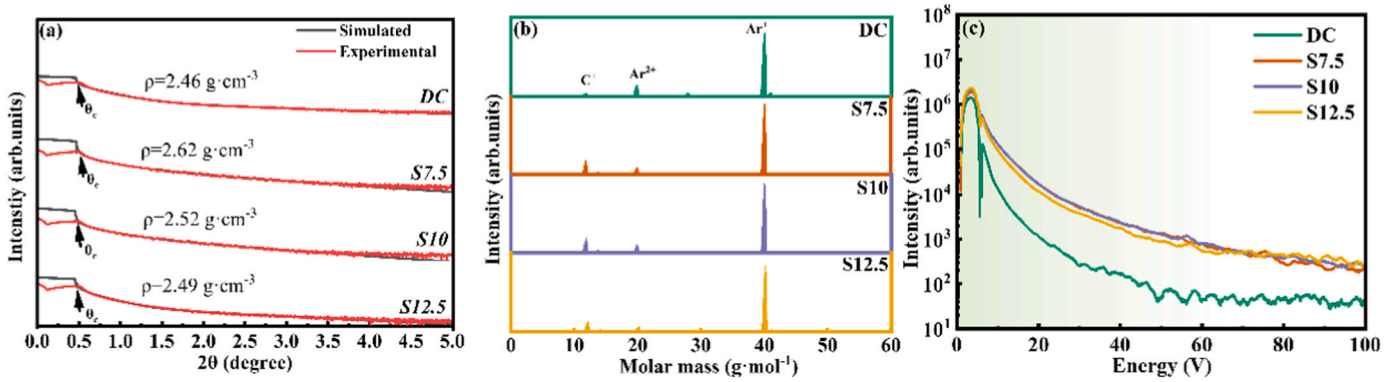

Fig. 4. (a) X-ray reflectivity data of Cr/GLC coatings with various duty cycles, (b) The mass spectra and (c) Time averaged IEDFs of representative carbon ions measured during sputtered graphite target by DCMS and HiPIMS.

energy of discharged C^+ ions than those in DCMS process. Such intensively energetic bombardment arisen from C^+ ions in turn promoted the achievement of compact structure with decreased growth defect like pinholes and rough surface, as well as the expected improvement of nanoindentation hardness in the HiPIMS-deposited carbon films [16]. Similar results were also obtained in our work, where the hardness and elastic modulus of HiPIMS-deposited coatings varied in range of 11.12–13.53 GPa and 190.51∼ 219.47 GPa, respectively, much higher than those of DCMS-deposited coating at 10.43 GPa and 176.25 GPa (Supporting information Fig. 1). Moreover, when the duty cycle in HiPIMS was 7.5%, the value of H/E reached the maximum of 0.06, indicating the strongest elastic exercise strain among all the coatings. Taking the combinational results of XPS and XRR as well as the plasma diagnostic investigation, the HiPIMS-deposited GLC coating presented the higher structure density with lower porosity and superior mechanical properties than those of DCMS-deposited ones, while the atomic bond structure was maintained at similar in both DCMS and HiPIMS discharge processes.

3.2. Electrochemical performance of Cr/GLC coatings

3.2.1. Polarization tests in atmospheric pressure

Fig. 5(a) shows the potentiodynamic polarization curves of various Cr/GLC coatings in 3.5 wt.% NaCl solutions. Different with the three-state characteristics of activation, passivation and break-down in the cathodic regions, all the samples showed the slanted lines with a small slope in the anodic regions, corresponding to the simultaneous passivation and solubilization. If one kept mind of the intrinsic inertness in amorphous carbon matrix, the passivation occurred in the anodic region could be induced by the growth defects of pinholes during sputtering GLC process, which in turn favored the possible anodic passivation in next Cr layer or even in bottom stainless-steel substrate [15,22]. Noted that increasing the duty cycle of HiPIMS, the corrosion potential of coated samples moved forward to the higher value, particularly the sample of S7.5 reached the highest potential. The Barnartt' s three-point method was used to fit the potentiodynamic polarization curves obtained from the Cr/GLC multilayer coatings based on the low-polarization region in an anode domain. Table 1 illustrated the fitting results involving the electrochemical properties. Comparing with the DCMS sample with the lowest corrosion potential (E_{corr}) at - 0.297 V and the highest corrosion current density (i_{corr}) at 7.9×10^{-7} A/cm^2, all the HiPIMS coated samples revealed the enhancement of corrosion resistance in view of the increase of E_{corr} and decrease of i_{corr}. However, noted that the corrosion resistance of coating was degraded with increasing the duty cycle from 7.5% to 12.5%. When the duty cycle of HiPIMS was 7.5%, the coating presented the best corrosion resistance with the highest E_{corr} at − 0.167 V and the lowest i_{corr} at 1.59×10^{-7} A/cm^2, approximately five times smaller than those of S7.5 and S10.

The polarization resistance (R_p) value of various coatings could be further estimated according to Stern-Geary equation[35,36]:

$$R_p = \frac{-\beta_a\beta_c}{2.303 i_{corr}(\beta_a+\beta_c)A} \quad (2)$$

Here, β_a and β_c were the slopes of the anode and the cathode, i_{corr} was the corrosion current density, A was assigned to the coating exposure area of 0.28 cm^2 in atmospheric polarization test. According to the calculated R_p, the corrosion speed of corrosive system could thereafter be elucidated comparatively. Furthermore, the coating porosity (P_p) was another important index to evaluate the corrosion resistance of coatings, which was generally calculated by the following equation[35,36]:

$$P_p = \left(\frac{R_{p(substrate)}}{R_{p(coating)}}\right) 10^{\left(-\frac{|\Delta E|}{\beta_a}\right)} \quad (3)$$

Here, $R_{p(substrate)}$ and $R_{p(coating)}$ were the polarization resistances of

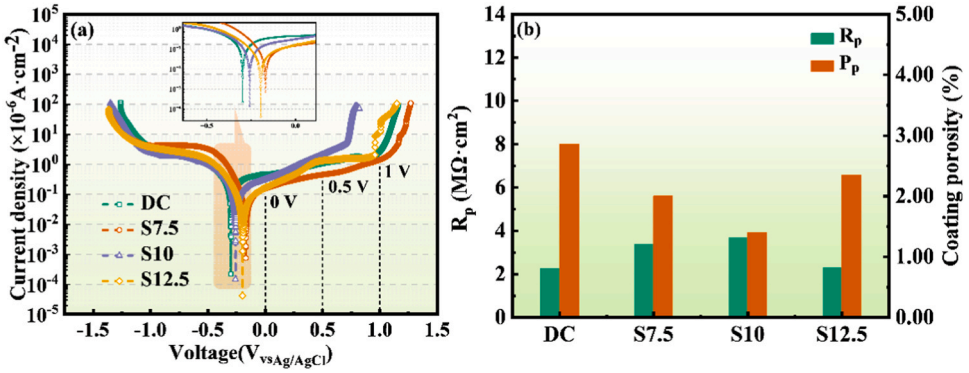

Fig. 5. (a) Potentiodynamic polarization curves, and (b) The calculated protective efficiency and porosity of the Cr/GLC coatings with different duty cycles.

Table 1
Fitted electrochemical parameters from potentiodynamic polarization tests for various Cr/GLC coatings under atmospheric pressure (AP) and hydrostatic pressure of 15 MPa.

Sample	E_{corr}/ V (vs $_{Ag/AgCl}$)		i_{corr} /10^{-7}A/ cm^2		β_a/V·decade^{-1}		-β_c /V·decade^{-1}	
	AP	15 MPa	AP	15 MPa	AP	15 MPa	AP	15 MPa
DC	-0.297	-0.253	7.9	8.74	3.22	0.69	0.81	0.31
S7.5	-0.167	-0.223	1.59	5.24	2.36	1.22	0.28	0.35
S10	-0.258	-0.209	1.65	2.56	1.40	0.88	0.29	0.24
S12.5	-0.194	-0.235	6.03	6.64	1.13	1.20	0.48	0.40

substrate and coating, respectively. |ΔE| was the absolute value of the self-corrosion potential difference between substrate and coating. While β_a was the Tafel slope of the anodic reaction during corrosion. According to Eqs. (2) and (3), the polarization resistance of R_p and porosity of P_p could be used to address the corrosion evolution for coatings (Fig. 5(b)). For the DCMS coating, R_p and P_p was 3.14 MΩ·cm^2 and 2.5%, respectively. Nevertheless, once the duct cycle of HiPIMS was applied with 7.5%, 10%, and 12.5% during GLC deposition, the polarization resistance R_p was increased to 5.03 MΩ·cm^2, 4.28 MΩ·cm^2, 6.03 MΩ·cm^2, respectively, which was about 60.1%, 36.3% and 92.0% of the data of DC sample. Meantime, the porosity of DCMS coated sample was reduced almost two times from 2.5% to the lowest range of 1.1–1.3% in HiPIMS-deposited samples.

3.2.2. *In-situ EIS results of immersion tests*

To gain insight into the corrosion evolution of Cr/GLC coatings in deep-sea environments, we conducted the EIS tests under various immersion periods in range of 0–425 h (Supporting information Fig. 2). For visual definition, Fig. 6 shows the Nyquist plots of different coatings with the representative four immersing times in simulated deep-sea environment with pressure of 15 MPa (corresponding to depth of 1500 m under sea). The inset image in each figure was the enlarged pattern from the marked yellow rectangle. As shown in Fig. 6, all Nyquist plots were characterized by a remarkable capacitance loop and a straight line in the whole frequency range, proposing a strong protective capability to suppress the hydrostatic corrosion. In general, the larger the capacitive loop diameter was, the better corrosion resistance was observed for the materials. It is found from each magnified figure that the first capacitance loop increased for all three samples, except for sample S7.5, when comparing 0 h and 29 h. Meanwhile, the area of diffusion was weakened. This represents the fact that the GLC layers of DC, S10, S12,5 are not dense enough to expose the Cr layer, which caused the Cr layer to generate a passivation layer, resulting in the Nyquist plots exhibiting a small enhancement. Nevertheless, it noted that increasing the immersion time to 185 h and 425 h led to a gradual decline trend of capacitive loops for each sample. The oblique line demonstrated that there might be an obvious substance transfer process with increase of the immersion for all Cr/GLC samples. It represents that the solution exerted a penetration effect and affects the barrier property of the coating. However, the capacitance arc of S7.5 decreased less compared to the other three samples. Therefore, it could be said that the HiPIMS-deposited coatings especially S7.5 performed the more excellent anti-corrosion properties than that of DCMS coated samples.

The Bode plots shown in Fig. 7 displayed that, with the extension of immersion time, all the phase angles in middle frequency (~10^0 Hz) shifted upward before 29 h. After that, the phase angles were stabilized with immersion time in range of 29–89 h. Beyond of 89 h, a reduction were observed in the phase angles, which further fell lower than the initial phase angle in 185 h. At intermediate frequency of 10^0 Hz, the phase angles of DC, S7.5, S10 and S12.5 coatings were evolved from

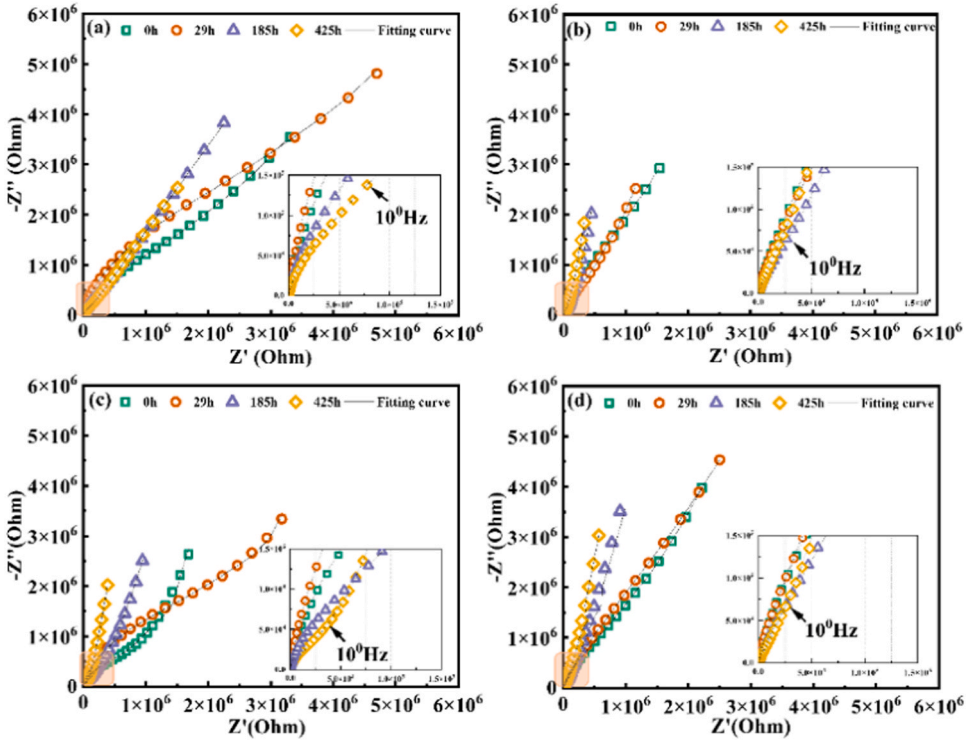

Fig. 6. In-situ Nyquist plot of (a) DC, (b) S7.5, (c) S10, and (d) S12.5 by sample different deposition methods under hydrostatic pressure of 15 MPa.

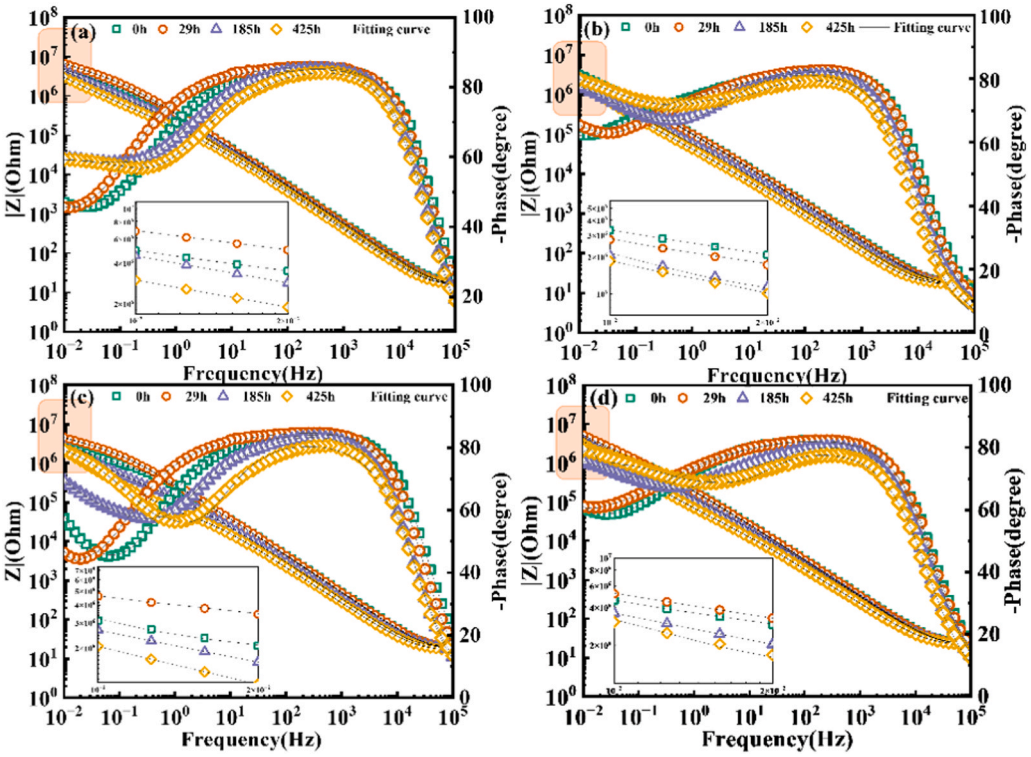

Fig. 7. In-situ Bode plot of (a) DC, (b) S7.5, (c) S10, and (d) S12.5 by different deposition methods under hydrostatic pressure of 15 MPa.

69.89°, 74.18°, 65.63° and 72.46°–60.56°, 72.01°, 56.33° and 68.98°, respectively. The decrease in phase angle represents a decrease in the capacitive properties of the coating, and the solution reached the metal through the defects, causing localised corrosion [37]. The absolute impedance value, |Z|, increased firstly at low frequency of 10^{-2} Hz and then decreased with the extended immersion. In the overall frequency region during EIS tests, the low-frequency capacitive region could be a sign to address the reaction occurred at the defective interface between

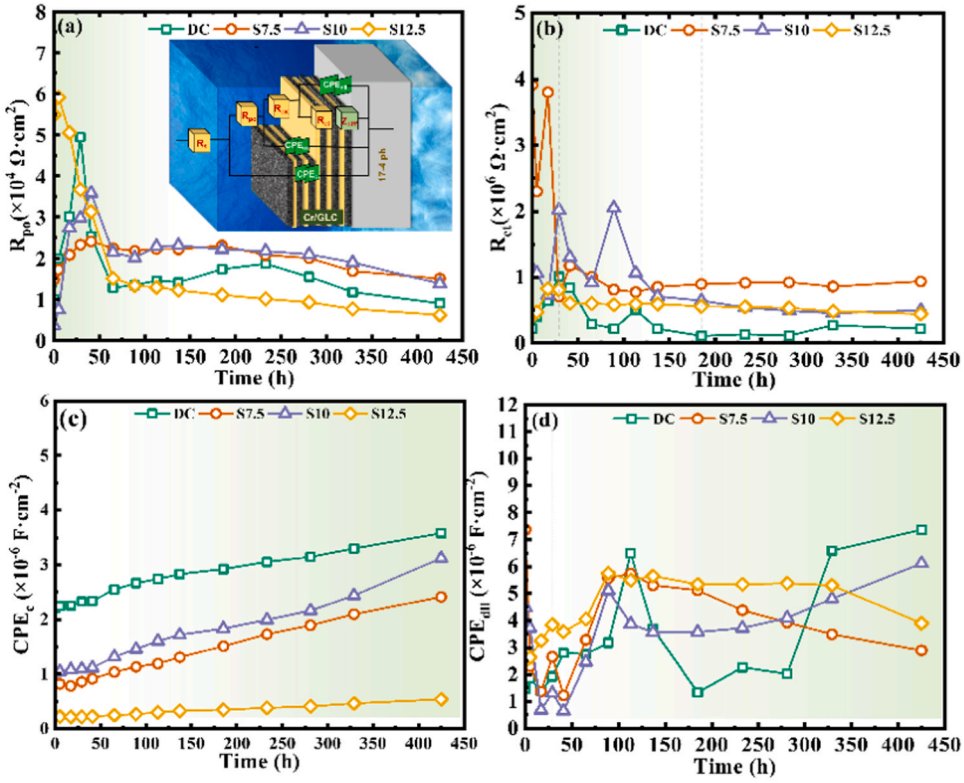

Fig. 8. The fitted values of (a) R_{po}, (b) R_{ct}, (c) CPE_c and (d) CPE_{dll} of Cr/GLC coatings deposited by different methods under 15 MPa hydrostatic pressures (the inserted image in (a) shows the equivalent electrical circuits for EIS fitting).

the electrolyte and substrate. As a result, the combined results of Nyquist and Bode plots clarified that the HiPIMS-deposited coatings exhibited the better corrosion resistance than the DCMS coating.

According to the Nyquist and Bode plots, all the Cr/GLC multilayer coatings illustrated the three time-constants evolution, which could be relatively fitted by the inserted equivalent circuits shown in Fig. 8(a). From the equivalent circuit, the R_s is the solution resistance, R_{ct} is the charge transfer resistance at the substrate surface, R_f was the oxides resistance of Cr layer, while R_{po} is the coating pore resistance. In addition, the constant phase element (*CPE*) is used instead of the pure capacitance, due to the "scattering effect" in coating system. For the given equivalent circuit, CPE_{dll} is relevant to the electric double layer capacitance between electrolyte and substrate, CPE_f is the capacitance of Cr layer while CPE_c represents the capacitance of the coating surface [22]. The Warburg impedance (Z_{diff}) represents the diffusion of corrosive chloride medium into the coating through growth defects of coating, where a corrosive reaction mainly occurred in the metallic interlayer of Cr. Most importantly, the Cr_2O_3 passivation layer could limit the mass transport of species, and the corresponding electrochemical reaction could be assigned to the Eq. (4) and (5).

$$Cr - 3e^- \rightarrow Cr^{3+} \tag{4}$$

$$2Cr + 3H_2O - 6e^- \rightarrow Cr_2O_3 + 6H^+ \tag{5}$$

Therefore, the R_{po}, R_{ct}, CPE_c and CPE_{dll} of the coatings could be deduced from the electrochemical impedance spectra. The values of fitted parameters and fitting accuracy were listed in Table S2-S5 for better understanding. The values of the electric double layer capacitance, CPE_{dll}, were calculated by Brug's formula [38]. The values of the CPE_c and CPE_f were calculated based on the work from Hsu's and Mansfeld's studies [39]. Fig. 8 shows the fitted values of R_{po}, R_{ct}, CPE_c and CPE_{dll} for the various Cr/GLC coatings after immersion 425 h under the hydrostatic pressure of 15 MPa. For both DCMS and HiPIMS coated samples, all the R_{po} was distinctly enhanced with immersion time up to 25 h, which might be attributed to the corrosive products filling the coating pores or the passivation layer generated on the Cr layer. During the immersion period of 25–65 h, it was found that all the R_{po} decreased to the initial value due to the passivation dissolved in the corrosive solution. Beyond of the immersion 75 h, a relatively stabilized curve was visible. Noted that as the duty cycle of HiPIMS increased, the coating R_{po} was reduced. Representatively, the averages R_{po} of the S7.5 coatings after stabilization were close to 2.05×10^4 Ω·cm^2, which were about 45% higher than that of DC coating. This was consistent well with the porosity calculated from the potentiodynamic polarization curve in the atmospheric environment.

Generally, R_{ct} indicated the charge transfer process across the interface of electrode/electrolyte solution, the higher R_{ct} reflected the stronger corrosion resistance and the slower corrosion reaction of system [40–42]. Fig. 8(b) displays the evolution of R_{ct} with the various immersion periods under high hydrostatic pressure of 15 MPa. During the early stage, a distinct fluctuation was observed in the curves, as an evidence of presence of coating pores. As a consequence, the corrosive medium could pass through the pores directly, which caused the easy corrosion of the Cr layer or the substrate for the process of passivation and re-passivation. After immersion for 100 h, the corrosion system was gradually stabilized, but the value of R_{ct} was varied significantly. Different with the smallest R_{ct} of 2.32×10^5 Ω·cm^2, R_{ct} was decreased with the increase of duty cycles in HiPIMS, where the largest R_{ct} of 8.86×10^5 Ω·cm^2 was obtained for the S7.5 sample. In other words, this result demonstrated that the HiPIMS-deposited Cr/GLC coatings at duty cycle of 7.5% performed the largest charge transfer resistance and a stronger ability preventing the aggressive ions reaching the interface of coating/substrate, which might be arisen from the high compactness and the strong bonded interfacial bilayer. The thicker the interfacial double layer was, the wider the depletion layer on the electrode surface was, which induced to the response reduction of the electrode interface [43].

CPE_c was well known related to the coating porosity. As shown in Fig. 8(c), a slight increase of CPE_c was illustrated from the start of immersion to the end of 425 h for each coating. Based on the empirical equations [22] , the higher value of CPE_c indicated a fast corrosion process during immersion, which could be closely related to the chemical composition and microstructure of multilayer coating system. After immersion for 425 h, the CPE_c of DC-deposited coating changed in a small range from 2.21×10^{-6} F·cm^{-2} to 3.58×10^{-6} F·cm^{-2}. However, the HiPIMS-GLC coated sample demonstrated the CPE_c at 2.41×10^{-6} F·cm^{-2}, 2.24×10^{-6} F·cm^{-2}, 5.37×10^{-7} F·cm^{-2} for S7.5, S10 and S12.5, respectively. Since the CPE_c here was strongly determined by the exposed area of the active area and the coating porosity, the results revealed that the active area with pores was intensively extended with enhanced immersion under 15 MPa.

Considering the evolution of electric double layer capacitance CPE_{dll}, Fig. 8(d) revealed the corrosion reaction for the coated substrate under immersion. Firstly, the CPE_{dll} decreased slowly and followed by a slight increase after 25 h immersion. Due to the conductive properties of the pristine 17–4 PH stainless steel, CPE_{dll} could be the main consequence of the exposed area occurred on the substrate, which could be subsequently deduced from the related equation as well [22]. All the CPE_{dll} fluctuated greatly with immersion time, but only a small variation was visible among DC and HiPIMS coated substrates. Moreover, a slow decline emerged on the evolution of CPE_{dll} at the immersion beginning, and followed by a fluctuation with a large amplitude after 25 h. However, noted that the coating of S7.5 showed the smallest corrosion response with range of immersion time at 250–425 h. According to equation, it can be introduced that electric double layer and electric double layer capacitance are mainly inversely proportional. A decrease in CPE_{dll} represents an increase in the thickness of the electric double layer. Hydrostatic pressure promoted the decrease in the thickness of the electric double layer as well as the adsorption of chloride ions [44]. The greater thickness of the electric double layer for HiPIMS sample as compared to DC meant that the corrosive medium was less likely to penetrate.

Based the abovementioned analysis on the combined definitions of R_p, R_{ct}, and CPE_c, the corrosion reaction of Cr/GLC multilayer coatings was dominated by the intermediate Cr layer and the exposed substrate originated from the coating pores. In particular, even the value of CPE_c of DC coating was bigger than that of S7.5, S10 and S12.5, the CPE_{dll} manifested the small difference of exposed area between substrates and the entirely Cr/GLC multilayer coatings deposited by various techniques, which indicated the corrosion reaction was more likely to form in Cr the layer. Alternatively, it could be concluded that the durability of corrosion resistance for all Cr/GLC coated substrates was highly stable.

3.2.3. Polarization tests under 15 MPa hydrostatic pressure

Fig. 9(a) shows the polarization curves of Cr/GLC coatings under 15 MPa hydrostatic pressure. In the anodic area, all curves demonstrated a slow upward trend with increase of applied potential. Considering the excellent chemical inertness of GLC coatings, such phenomenon could be mainly assigned to the dissolution and re-passivation from Cr layers. Specially, increasing the potential from 1.0 V to 1.3 V led to the firstly decrease and substantial increase in the current density, identifying the rupture of the carbon layer and passivation of the metal in high hydrostatic pressure (enlarged view in Fig. 9 (a)). After fitting the potentiodynamic polarization curves by Barnartt's three-point method, the electrochemical parameters during corrosion were clarified in Table 1 and Fig. 9(b). The related exposed areas have been shown in the SI (Fig. 3). Obviously, all the HiPIMS-deposited coatings exhibited the higher corrosion potentials and lower corrosion current densities than that of DC-deposited coating with E_{corr} at − 0.253 V and i_{corr} at 8.74×10^{-7} A/ cm^2. In particular, the minimum i_{corr} of S10 sample was almost reduced four times comparing to that of DC case, which indicated the quite lower corrosion rate and thereafter the enhancement of corrosion resistance. However, noted that, unlike

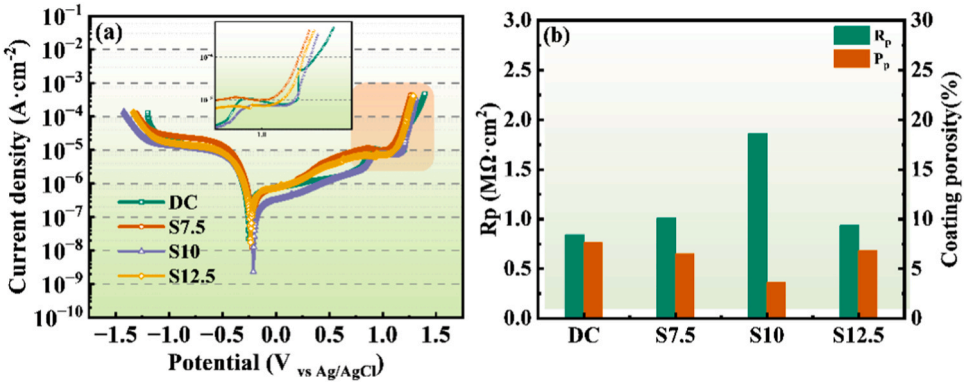

Fig. 9. Potentiodynamic polarization curves of the various Cr/GLC coatings under hydrostatic pressures.

the corrosion behavior under atmospheric pressure, the polarization resistance, R_p, was 1.86 MΩ·cm^2 under 15 MPa hydrostatic pressure for S10 sample, which was about 2.2, 1.7 and 1.8 times larger than that of DC, S7.5 and S12.5, respectively. As for the coating porosity, S10 sample illustrated the porosity of P_p at 3.6%, being much smaller than that of DC-7.6% and HiPIMS deposited samples of S7.5–6.5%, and S12.5–6.8%, respectively.

3.2.4. *Morphology after corrosion polarization*

In order to explain the above phenomenon, by observing the surface morphology of samples after polarization test in the deep sea. Fig. 10 shows the representatively corrosive morphology of coatings after the polarization test under high hydrostatic pressure of 15 MPa for 425 h. Except of the small amount of NaCl particles, no observation of corrosive defects and coating spallation was visible for the DC coated sample. However, the HiPIMS-deposited Cr/GLC coatings manifested the much severer annular spallation and even delamination from the coatings, which was in contrast to the better corrosion performance suggested by EIS and polarization results. Furthermore, the delamination area enlarged from the orange circle in Fig. 11(d) was mainly comprised of Cr element. This identified the coatings were preferred peeling off from the interface between Cr layer and GLC layers. Comparing to the difference between DC and HiPIMS samples, as a result, the anti-corrosion degradation and porosity increase in HiPIMS-deposited coatings could be understood from two aspects. Firstly, under high hydrostatic pressure, liquids are more likely to enter the interface of the coating, which in parallel easily stimulated the formation of galvanic corrosion reaction at interfaces. Secondly, different with the lower ionization rate and ion energy in DC process, the discharge plasma was highly ionized and the incident ion energy were much larger in HiPIMS approach, which favored the heavier kinetic ion bombardment during GLC layer growth. However, according to the combined simulations and experiments, the high incident plasma energy yielded the highly dense structure of coatings, but the heavy bombardment with high incident energy also easily led to the strongly structural distortion and the consequence of high compressive stress within interfaces in multilayered coating. This resulted in the densely structure to suppress the anti-corrosion, while accompanying with the higher residual compressive stress in coatings.

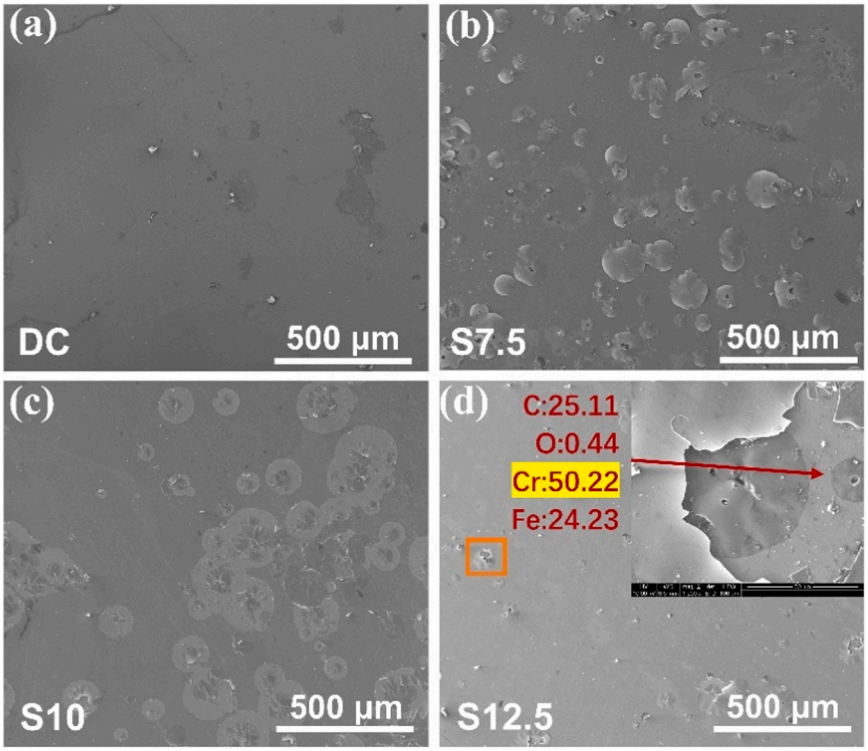

Fig. 10. Surface morphologies of (a) DC, (b) S7.5, (c) S10, (d) S12.5 after potentiodynamic under 15 MPa hydrostatic pressures.

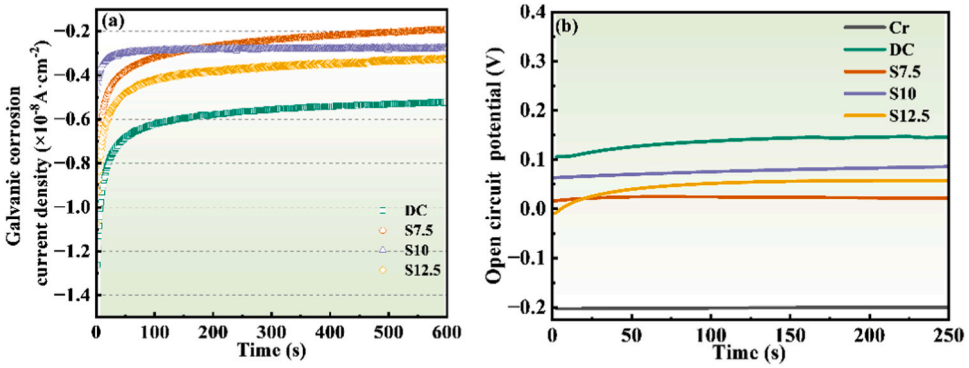

Fig. 11. (a) Galvanic corrosion current density between Cr and GLC, and (b) OCP of Cr and GLC coatings deposited by different methods.

Finally, the high residual cracks in coating were accelerated by the high hydrostatic pressure of 15 MPa and large potential, stimulating the critical corrosion damage in HiPIMS samples than that of DC case.

3.3. Discussion

Based on the results of the above experiments, we found that HiPIMS maintained the lowest corrosion current density in both deep-sea environments and at atmospheric pressure, and even exhibits high porosity in deep-sea conditions. In order to reveal the reason for this phenomenon we have investigated the galvanic corrosion of the coatings. Most studies had reported that, once two metals with different corrosion potentials were in direct contact, the metal with the lower corrosion potential would dissolute rapidly as anode [45,46]. In current case, as the corrosive solution contacted the interface between the multilayer coating and substrate through the pore defects, the corrosion rate of the Cr interlayer would be accelerated significantly, due to the lower corrosion potential of Cr than that of GLC layer. Therefore, the corrosion of the Cr interlayer within the Cr/GLC multilayer coating could be alternatively the key factor to dominate the corrosion behavior.

Fig. 11(a) shows the galvanic corrosion current density between metallic Cr interlayer and GLC carbon layer in 3.5 wt.% NaCl. Particularly, the Cr coating acted as the reference electrode, while the GLC coating behave the working electrode. The results indicated that there was a negative corrosion current, identifying the appearance of Cr corrosion. If the current difference between anodic and cathodic electrodes was denoted as I_g, the value of I_g for Cr/GLC (DC mode) galvanic couple was stabilized at -5.3×10^{-9} A·cm^{-2}, while it was enhanced to the data of -2.04×10^{-9} A·cm^{-2}, -2.78×10^{-9} A·cm^{-2} and -3.36×10^{-9} A·cm^{-2} for the galvanic pair of Cr/GLC (S7.5), Cr/GLC (S10) and Cr/GLC (S12.5), respectively. Considering with the same characteristics of Cr layer during both DC and HiPIMS process, the decrease of the galvanic corrosion current density in hybrid HiPIMS technique were preliminary indications of the reduction of galvanic corrosion between Cr/GLC layers. To elucidate the dependence of galvanic corrosion upon the GLC feature, Fig. 11(b) shows the open circuit potential (OCP) vs. time for the Cr/GLC coatings deposited by various methods. It was clear that the self-corrosion potential of Cr layer was about − 0.2 V, but it was increased to 0.125 V for GLC (DC) and 0.02 V, 0.06 V, 0.045 V for GLC (S7.5), GLC (S10) as well GLC (S12.5), respectively. In general, the galvanic corrosion rate of contacted galvanic pairs was closely related to the driving force, known as the electromotive force, which was equal to the difference of self-corrosion potentials for the galvanic pair. The larger the driving force was, the higher corrosion rate could be reached [45]. Furthermore, if all the exposed area of metal, the corrosive solution resistance and the resistance of external circuit were maintained, the large electromotive force proposed the stronger accelerated corrosion effect during corrosive environment. In the present work, GLC (DC) presented the slight damaged morphology but accompanying the highest potential and larger galvanic corrosion current density. As for the case of HiPIMS-deposited GLC coatings, the sample of S7.5 demonstrated particularly the lower potential together with the weaker galvanic corrosion, even following with the serious damage occurred in the interfaces. This reveals the reason why the coating prepared by HiPIMS maintained low current density despite the damage.

For more direct understanding, based on the combinational characteristics of surface morphology and electrochemical corrosion results, Fig. 12 summarized the failure mechanism and excellent corrosion protection of Cr/GLC coatings prepared by DC and HiPIMS approaches for comparison. Thanks to the higher plasma ionization and larger incident ion energy for carbon species induced by high impulse power supply, the HiPIMS-deposited coating exhibited the high density of 2.62 g/cm^3 than the DC coating at 2.46 g/cm^3, indicating an increase of structural compactness. Most important, noted that the carbon atomic bonds in all Cr/GLC coatings was kept almost constant regardless of the density variations. Under the hydrostatic pressure of 15 MPa with long immersion time of 425 h in 3.5 wt.% NaCl solution, it was undeniable that the heavy ion bombardment accompanying with large compressive stress also led to the annular spallation in HiPIMS coatings [47]. This coincides with the the G-FWHM in Fig. 3(b). But, the enhanced compactness within HiPIMS-deposited multilayer coating significantly suppressed the direct diffusion of corrosive chloride medium, in which the i_{corr} of S7.5 was about 1.59×10^{-7} A/cm^2, being five times larger than that of DC coatings at 7.9×10^{-7} A/cm^2. At the same time, the galvanic corrosion between amorphous carbon layer and chromium layer was distinctly decreased about 3 times in HiPIMS process (I_g= 2.0×10^{-9} A/cm^2) comparing to the case of DC sample with I_g at 6.0×10^{-9} A/cm^2. As state above, the Cr/GLC coatings prepared by HiPIMS maintained good corrosion resistance even when damage occurred, increasing the damage tolerance of the coatings during

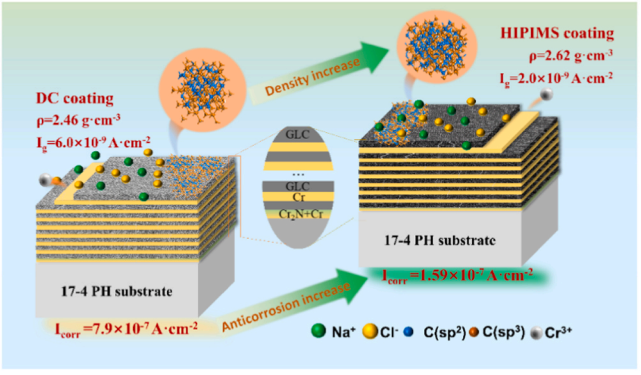

Fig. 12. Schematic diagram of the corrosion protection mechanism of Cr/GLC coatings prepared by HiPIMS and DC process for comparison.

long-term service. Therefore, if one kept mind of the contribution from coating density and porosity, the HiPIMS technique employing the high pulsed and instantaneous peak power would be an alternatively promising strategy to optimize the coating microstructure without simultaneous deterioration of atomic carbon bonds, which could favor the expected corrosion performance for advanced carbon coatings.

4. Conclusion

In this work, we fabricated a series of Cr/GLC multilayer coatings with thickness around 1.7–1.9 μm by DCMS and HiPIMS technology for comparison. The results showed that, with the same applied sputtering power, HiPIMS process significantly increased the ionization rate and incident ion energy than those of DCMS case. As the consequence, all the HiPIMS-deposited GLC coatings presented the larger density than the DC sample at 2.46 g/cm^3, where the HiPIMS-deposited S7.5 sample particularly behaved the maximum density at 2.62 g/cm^3. Thanks to the distinct improvement of coating density and compact structure as diffusion barrier for chloride medium, all the HiPIMS-deposited coatings enhanced the corrosion resistance with minimum i_{corr} at 2.56 × 10^{-7} A/cm^2 than that of DC sample at 8.74 × 10^{-7} A/cm^2 under the simulated deep-sea condition with 15 MPa pressure. However, noted that the various potentials between Cr/GLC layers with pore defects played the key role in the galvanic corrosion under high pressure in 3.5 wt.% NaCl solutions. In contrast to the DC sample, the galvanic corrosion current density between Cr/GLC interface was reduced about 3 times by HiPIMS technique due to the enhancement of coating density with less defects. Beyond of the above merits of HiPIMS coatings, the reason behind of the long-term corrosive degradation was predominately ascribed to the existence of high compressive stress within Cr/GLC coatings and facile cracks originated from the heavy ion bombardment with highly ionized C^+ ions species. In this viewpoint, it would be a critical challenge to both improve the corrosion resistance with long life-time and the strong durability over wide range of hydrostatic pressure for harsh marine components in future.

CRediT authorship contribution statement

Shuyu Li and **Hao Li** contributed to this work equally. **Shuyu Li**: Conceptualization, Methodology Investigation, Formal analysis, Validation, Writing – original draft. **Hao Li**: Validation. **Guanshui Ma**: Validation. **Jing Wei:** Validation. **Guangxue Zhou**: Methodology. **Yan Zhang**: Software. **Peng Guo**: Methodology Investigation, Validation. **Peiling Ke**: Editing, Funding acquisition. **Aiying Wang**: Writing – review & editing, Funding acquisition, Supervision.

Declaration of Competing Interest

We have no conflicts of interest to this work.

Data Availability

No data was used for the research described in the article.

Acknowledgements

This work was financial supported by the National Key Research and Development Program of China (2022YFC2805701), National Science Found for Distinguished Young Scholars of China (52025014), A-class pilot of the Chinese Academy of Sciences (XDA22010303), Ningbo Science and Technology Innovation Project (2023Z009) and Director's Fund of Ningbo Institute of Materials Technology and Engineering, (CAS2022SZKY0203).

Appendix A. Supporting information

Supplementary data associated with this article can be found in the online version at doi:10.1016/j.corsci.2023.111618.

References

[1] P. Traverso, E. Canepa, A review of studies on corrosion of metals and alloys in deep-sea environment, Ocean Eng. 87 (2014) 10–15.
[2] J. Liu, X.B. Li, J. Wang, T.Y. Luo, X.M. Wang, Studies of impedance models and water transport behaviours of epoxy coating at hydrostatic pressure of seawater, Prog. Org. Coat. 76 (2013) 1075–1081.
[3] Y. Liu, L. Liu, S. Li, R. Wang, P. Guo, A. Wang, P. Ke, Accelerated deterioration mechanism of 316L stainless steel in NaCl solution under the intermittent tribocorrosion process, J. Mater. Sci. Technol. 121 (2022) 67–79.
[4] J.H. Potgieter, P.A. Olubambi, L. Cornish, C.N. Machio, E.S.M. Sherif, Influence of nickel additions on the corrosion behaviour of low nitrogen 22% Cr series duplex stainless steels, Corros. Sci. 50 (2008) 2572–2579.
[5] A. Pardo, M.C. Merino, M. Carboneras, F. Viejo, R. Arrabal, J. Munoz, Influence of Cu and Sn content in the corrosion of AISI 304 and 316 stainless steels in H_2SO_4, Corros. Sci. 48 (2006) 1075–1092.
[6] H.S. Noh, J.H. Kang, K.M. Kim, S.J. Kim, The effect of carbon on hydrogen embrittlement in stable Cr-Ni-Mn-N austenitic stainless steels, Corros. Sci. 124 (2017) 63–70.
[7] L. Liu, Y. Cui, Y. Li, T. Zhang, F. Wang, Failure behavior of nano-SiO_2 fillers epoxy coating under hydrostatic pressure, Electrochim. Acta 62 (2012) 42–50.
[8] Y. Liu, J. Wang, L. Liu, Y. Li, F. Wang, Study of the failure mechanism of an epoxy coating system under high hydrostatic pressure, Corros. Sci. 74 (2013) 59–70.
[9] J. Robertson, Diamond-like amorphous carbon, Mat. Sci. Eng. R. 37 (2002) 129–281.
[10] J. Wei, P. Guo, H. Li, P. Ke, A. Wang, Insights on high temperature friction mechanism of multilayer ta-C films, J. Mater. Sci. Technol. 97 (2022) 29–37.
[11] X. Sui, R. Xu, J. Liu, S. Zhang, Y. Wu, J. Yang, J. Hao, Tailoring the tribocorrosion and antifouling performance of (Cr, Cu)-GLC coatings for marine application, ACS Appl. Mater. Interfaces 10 (2018) 36531–36539.
[12] C. Wang, Y. Ye, X. Guan, J. Hu, Y. Wang, J. Li, An analysis of tribological performance on Cr/GLC film coupling with Si_3N_4, SiC, WC, Al_2O_3 and ZrO_2 in seawater, Tribol. Int. 96 (2016) 77–86.
[13] P. Panjan, M. Čekada, M. Panjan, D. Kek-Merl, Growth defects in PVD hard coatings, Vacuum 84 (2009) 209–214.
[14] L. Li, P. Guo, L.-L. Liu, X. Li, P. Ke, A. Wang, Structural design of Cr/GLC films for high tribological performance in artificial seawater: Cr/GLC ratio and multilayer structure, J. Mater. Sci. Technol. 34 (2018) 1273–1280.
[15] Y. Liu, S. Li, H. Li, G. Ma, L. Sun, P. Guo, P. Ke, K.-R. Lee, A. Wang, Controllable defect engineering to enhance the corrosion resistance of Cr/GLC multilayered coating for deep-sea applications, Corros. Sci. 199 (2022), 110175.
[16] T. Kubart, A. Aijaz, J. Andersson, F. Ferreira, J.C. Oliveira, A. Sobetkii, A.C. Parau, C. Vitelaru, High power impulse magnetron sputtering of diamond-like carbon coatings, J. Vac. Sci. Technol. A 38 (2020), 043408.
[17] A. Anders, A review comparing cathodic arcs and high power impulse magnetron sputtering (HiPIMS), Surf. Coat. Tech. 257 (2014) 308–325.
[18] M.W. Qureshi, X. Ma, G. Tang, B. Miao, J. Niu, Fabrication and mechanical properties of Cr_2AlC MAX phase coatings on TiB_w/Ti6Al4V composite prepared by HiPIMS, Materials 14 (2021) 826.
[19] Z. Li, G. Zhou, Z. Wang, J. Yuan, P. Ke, A. Wang, HiPIMS induced high-purity Ti_3AlC_2 MAX phase coating at low-temperature of 700 °C, J. Eur. Ceram. Soc. 43 (2023) 4673–4683.
[20] L. Wang, J. Jin, C. Zhu, G. Li, X. Kuang, K. Huang, Effects of HiPIMS pulse-length on plasma discharge and on the properties of WC-DLC coatings, Appl. Surf. Sci. 487 (2019) 526–538.
[21] L. Wang, L. Li, X. Kuang, Effect of substrate bias on microstructure and mechanical properties of WC-DLC coatings deposited by HiPIMS, Surf. Coat. Technol. 352 (2018) 33–41.
[22] Y. Liu, H. Du, X. Zuo, P. Guo, L. Liu, K.-R. Lee, A. Wang, P. Ke, Cr/GLC multilayered coating in simulated deep-sea environment: Corrosion behavior and growth defect evolution, Corros. Sci. 188 (2021), 109528.
[23] X. Li, L. Li, D. Zhang, A. Wang, Ab initio study of interfacial structure transformation of amorphous carbon catalyzed by Ti, Cr, and W transition layers, ACS Appl. Mater. Interfaces 9 (2017) 41115–41119.
[24] L. Li, L.L. Liu, X. Li, P. Guo, P. Ke, A. Wang, Enhanced tribocorrosion performance of Cr/GLC multilayered films for marine protective application, ACS Appl. Mater. Interfaces 10 (2018) 13187–13198.
[25] X. Zhou, S. Tunmee, T. Suzuki, P. Phothongkam, K. Kanda, K. Komatsu, S. Kawahara, H. Ito, H. Saitoh, Quantitative NEXAFS and solid-state NMR studies of sp^3/ (sp^2 + sp^3) ratio in the hydrogenated DLC films, Diam. Relat. Mater. 73 (2017) 232–240.
[26] D. Persson, D. Thierry, N. LeBozec, T. Prosek, In situ infrared reflection spectroscopy studies of the initial atmospheric corrosion of Zn–Al–Mg coated steel, Corros. Sci. 72 (2013) 54–63.
[27] L. Liu, T. Wang, J. Huang, Z. He, Y. Yi, K. Du, Diamond-like carbon thin films with high density and low internal stress deposited by coupling DC/RF magnetron sputtering, Diam. Relat. Mater. 70 (2016) 151–158.

[28] J. Wei, P. Guo, L. Liu, H. Li, H. Li, S. Wang, P. Ke, H. Saito, A. Wang, Corrosion resistance of amorphous carbon film in 3.5 wt% NaCl solution for marine application, Electrochim. Acta 346 (2020), 136282.
[29] H. Sakata, G. Dresselhaus, M.S. Dresselhaus, M. Endo, Effect of uniaxial stress on the Raman spectra of graphite fibers, J. Appl. Phys. 63 (1988) 2769–2772.
[30] M. Ouchabane, C. Dublanche-Tixier, D. Dergham, Nanoindentation data analysis of loading curve performed on DLC thin films: Effect of residual stress on the elasto-plastic properties, J. Appl. Phys. 122 (2017), 175103.
[31] H. Li, P. Guo, D. Zhang, L. Liu, Z. Wang, G. Ma, Y. Xin, P. Ke, H. Saito, A. Wang, Interface-induced degradation of amorphous carbon films/stainless steel bipolar plates in proton exchange membrane fuel cells, J. Power Sources 469 (2020), 228269.
[32] P. Maheshwari, D. Bhattacharya, S.K. Sharma, S. Mukherjee, S. Samanta, S. Basu, D.K. Aswal, P.K. Pujari, Probing inhomogeneities in nanoscale organic semiconductor films: Depth profiling using slow positron beam and X-ray reflectivity techniques, Solid State Commun. 200 (2014) 22–28.
[33] N. Konkhunthot, S. Tunmee, X. Zhou, K. Komatsu, P. Photongkam, H. Saitoh, P. Wongpanya, The correlation between optical and mechanical properties of amorphous diamond-like carbon films prepared by pulsed filtered cathodic vacuum arc deposition, Thin Solid Films 653 (2018) 317–325.
[34] F. Ferreira, C. Sousa, A. Cavaleiro, A. Anders, J. Oliveira, Phase tailoring of tantalum thin films deposited in deep oscillation magnetron sputtering mode, Surf. Coat. Tech. 314 (2017) 97–104.
[35] A.L.G. M.Stern, Electrochemical polarization: I. a theoretical analysis of the shape of polarization curves, J. Electrochem. Soc. 104 (1957) 8.
[36] K.A.Katsuhisa Nozawa, One- and two-dimensional polymer films of modified alkanethiol monolayers for preventing iron from corrosion, Corros. Sci. 41 (1999) 57–73.
[37] M. Mouanga, P. Berçot, Comparison of corrosion behaviour of zinc in NaCl and in NaOH solutions; Part II: Electrochemical analyses, Corros. Sci. 52 (2010) 3993–4000.
[38] G.J. Brug, A.L.G.V. Eeden, M. Sluyters-Rehbach, J.H. Sluyters, The analysis of electrode impedances complicated by the presence of a constant phase element, J. Electroanal. Chem. 176 (1984) 275–295.
[39] C.H. Hsu, F. Mansfeld, Concerning the conversion of the constant phase element parameter Y_0 into a capacitance, Corrosion 57 (2001) 747–748.
[40] C.O.A. Olsson, D. Landolt, Passive films on stainless steels—chemistry, structure and growth, Electrochim. Acta 48 (2003) 1093–1104.
[41] S. Khamseh, E. Alibakhshi, B. Ramezanzadeh, J.-S. Lecomte, P. Laheurte, X. Noirefalize, F. Laoutid, H. Vahabi, Tailoring hardness and electrochemical performance of TC4 coated Cu/a-C thin coating with introducing second metal Zr, Corros. Sci. 172 (2020), 108713.
[42] F.M.C.H. Tsai, Determination of coating deterioration with EIS: I. basic relationships, Corrosion 47 (1991) 5.
[43] R. Liu, Y. Cui, L. Liu, F. Wang, Study on the mechanism of hydrostatic pressure promoting electrochemical corrosion of pure iron in 3.5% NaCl solution, Acta Mater. 203 (2021), 116467.
[44] H. Ma, R. Liu, Y. Cui, P. Ke, F. Wang, L. Liu, The effect law of different hydrostatic pressures on the failure of multilayer Cr/GLC coatings in 3.5.wt% NaCl solution, Corros. Sci. 217 (2023), 111120.
[45] J. Qiu, A. Wu, Y. Li, Y. Xu, R. Scarlat, D.D. Macdonald, Galvanic corrosion of type 316L stainless steel and graphite in molten fluoride salt, Corros. Sci. 170 (2020), 108677.
[46] E. Ilic, A. Pardo, T. Suter, S. Mischler, P. Schmutz, R. Hauert, A methodology for characterizing the electrochemical stability of DLC coated interlayers and interfaces, Surf. Coat. Technol. 375 (2019) 402–413.
[47] X. Li, P. Ke, H. Zheng, A. Wang, Structural properties and growth evolution of diamond-like carbon films with different incident energies: a molecular dynamics study, Appl. Surf. Sci. 273 (2013) 670–675.